Sensorless Synchronous Reluctance Motor Drives: A Projection Vector Approach for Stator Resistance Immunity and Parameter Adaptation

(Article begins on next page)

04 May 2024

Sensorless Synchronous Reluctance Motor Drives: A Projection Vector Approach for Stator Resistance Immunity and Parameter Adaptation

Anantaram varatharajan and Gianmario Pellegrino, *Senior Member, IEEE,*

Abstract—The paper presents a general projection vector framework for the analysis of flux and position observers applied to sensorless control of synchronous reluctance machines, with emphasis to parametric errors sensitivity. The stator resistance immunity property of Adaptive Projection vector for Position error estimation (APP) technique is demonstrated, in maximum torque per ampere (MTPA) conditions. Out of MTPA, additional resistance adaption is devised for accurate estimation of stator flux and torque. Alternatively, inductance adaptation might be preferred to resistance's, when dealing with inaccurate motor flux-maps. Inductance adaptation is shown to decrease the steady-state position error. All proposed APP observers with adaptation techniques are subjected to stability analysis. The merit and the feasibility of the proposed scheme is experimentally demonstrated on a 1.1 kW synchronous reluctance (SyR) machine test-bench.

Index Terms—Sensorless control, adaptive projection vector, stator resistance adaptation, inductance adaptation, synchronous reluctance machine.

I. INTRODUCTION

Owing to the saliency of synchronous reluctance (SyR) machine, the position and speed estimation without an encoder or resolver becomes realizable. The literature contains numerous works on high frequency signal injection methods in different reference frames for operation at low and zero speeds region [1] [2]; [3] presents a comprehensive review of high frequency injection techniques. Fundamental wave excitation based approach is preferred at medium and high speeds [4] [5]; fusion methods are available for smooth transition between low and high speed methods [6] [7]. The proposed technique falls in the latter category and can be augmented with high frequency injection schemes for covering the full speed range of the electrical drive. This paper proposes a new sensorless control scheme based on the Adaptive Projection vector for Position error estimation (APP), with immunity to stator resistance detuning under maximum torque per ampere (MTPA) conditions, and with online parameter adaptation capability.

The flux and position observers are susceptible to resistance variation at low speeds, leading to steady-state posi-

tion error and even instability. To circumvent this, several methods have been explored: stator resistance observers for non-salient synchronous machines are proposed in [8]; sliding mode observers are developed in [9]; a recursive least square approach is resorted to identify resistance online in [10]. Besides stator resistance, errors in motor inductances or flux-maps are critical in sensorless applications, leading to the inevitable position error and potential instability. Sensorless self-commissioning techniques for standstill identification of flux-maps are reported in [11], [12]. Permanent magnet flux adaptation for sensorless synchronous machines is reported in [13]. An inductance error adaptation for improved torque accuracy in permanent magnet machines is proposed in [4]. A high frequency injection based inductance adaptation is proposed in [14] for PM synchronous motors with linear magnetic model. To the author's knowledge, the inductance adaptation in sensorless SyR motor drives is not widely reported.

The projection vector approach is a unified design and analysis framework for a class of fundamental wave excitation based sensorless observers, first explored in [5]. Many commonly used sensorless techniques rely on the discrepancy between observed and current model flux estimates; this discrepancy is a 2-D domain (dq) where the error can be minimized along any of the infinite directions for position tracking. Minimizing the q-axis error is the well-known active-flux observer approach which can be represented as a subset within the projection vector framework. In [15], the stability analysis of active-flux based position observer is reviewed and discussed using the same framework, and a new Adaptive Projection vector for Position error estimation (APP) is developed, circumventing the risk of instability in braking and overload conditions of the active-flux approach.

A. Varatharajan and G. Pellegrino are with the Department of Energy, Politecnico di Torino, Turin 10129, Italy. (email: anantaram.varatharajan@polito.it; gianmario.pellegrino@polito.it)
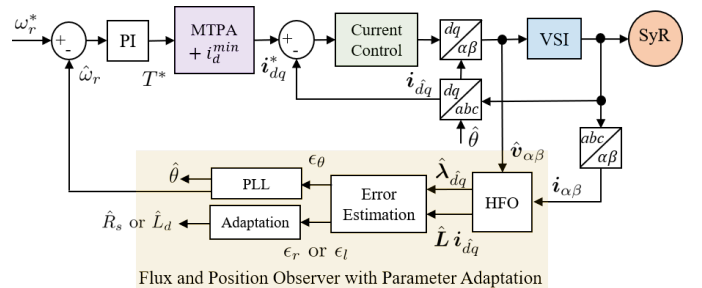
Fig. 1. Control system overview illustrating the hybrid flux observer (HFO) and position observer augmented with parameter adaptation.

Moreover, the stator resistance immunity property of APP technique is demonstrated in [16]. This work further develops on conference work [16] with an elaborate sensitivity analysis to parameter errors. Finally, an inductance adaption scheme is devised to replace resistance adaption in the presence of inaccurate flux-maps, which is entirely a new contribution of this work.

Section II introduces the machine model and the analysis of flux observer. Section III presents the generic projection vector framework for sensorless control system and develops the proposed APP technique. Section IV and V describes the parameter adaptation and stability analysis, respectively. The main contributions of the paper are summarized as follows:

1) A position observer based on Adaptive Projection vector for Position error estimation (APP) [15] is developed to demonstrate the immunity to resistance error for operating points respecting MTPA law.
2) The immunity also extends to the voltage error due to non-ideal compensation of inverters as the fundamental component of voltage error is in phase with the stator current [17].
3) The auxiliary flux linkage vector is defined and the general property of such vector being aligned to the current vector along MTPA is established.
4) A stator resistance adaption is developed to alleviate the steady-state position error at non-MTPA operating points; furthermore, it aids in accurate estimation of stator flux and torque.
5) Alternatively, an inductance adaptation is proposed for operations under parametric error in flux-maps, resulting in a reduced position error.
6) The observers with resistance/inductance adaptation are subjected to stability analysis.

The section VI covers the experimental validation of proposed method with a 1.1 kW SyR motor drive.

II. SENSORLESS CONTROL SYSTEM

The electrical rotor position is θ and the electrical angular speed is $\omega = s\,\theta$ where s is the differential operator $\frac{d}{dt}$. Estimated vectors are represented by the superscript ˆ. The orthogonal rotational matrix is $\mathbf{J} = \begin{bmatrix} 0 & -1 \\ 1 & 0 \end{bmatrix}$ and $\mathbf{I}$ is the identity matrix.

The machine model is expressed in coordinates of estimated rotor reference frame, denoted by subscript $\hat{d}q$, whose d-axis is at $\hat{\theta} = \theta - \tilde{\theta}$, where $\tilde{\theta}$ is the position error. Real space vectors will be used; for example, the stator current is $\boldsymbol{i}_{\hat{d}q} = [i_{\hat{d}}, i_{\hat{q}}]^{\mathrm{T}}$ where $i_{\hat{d}}$ and $i_{\hat{q}}$ are the vector components in estimated rotor reference frame. Space vectors in stationary reference frame are denoted by subscript $\alpha\beta$.

The block diagram illustrating an overview of the motor control is shown in the Fig.1.

A. Synchronous Reluctance Motor Model

The voltage equation of a SyR machine in estimated rotor reference frame is expressed as

$$s\,\boldsymbol{\lambda}_{\hat{d}q} = \boldsymbol{v}_{\hat{d}q} - R_s \boldsymbol{i}_{\hat{d}q} - \hat{\omega}\,\mathbf{J}\,\boldsymbol{\lambda}_{\hat{d}q} \qquad (1)$$
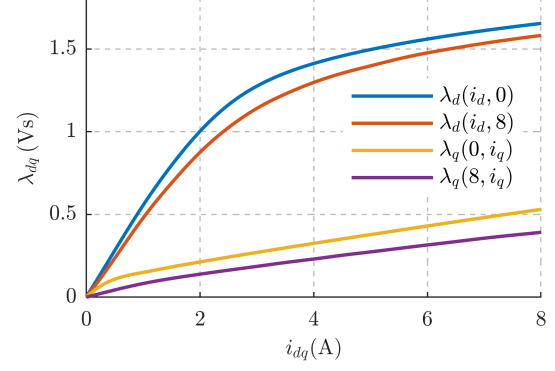

Fig. 2. Experimentally obtained flux maps LUTs of the 1.1 kW SyR motor under test: $\boldsymbol{\lambda}_{dq} = \boldsymbol{\Lambda}_{dq}(\boldsymbol{i}_{dq})$

where R_s is the stator resistance and $\boldsymbol{\lambda}_{\hat{d}q}$ is the stator flux linkage. The electromagnetic torque is given by

$$T = \frac{3p}{2}\,\boldsymbol{i}_{\hat{d}q}^{\mathrm{T}}\,\mathbf{J}\,\boldsymbol{\lambda}_{\hat{d}q} \qquad (2)$$

where p is the number of pole pairs.

B. Inductance Modeling in Sensorless Control

The SyR machine under test is commissioned using constant speed test reported in [18] for flux map identification, shown in Fig. 2. Let the 2-D flux map lookup tables (LUTs) be denoted by $\boldsymbol{\Lambda}_{dq}$. Then, the stator flux in estimated rotor reference frame is expressed as

$$\boldsymbol{\lambda}_{\hat{d}q} = \mathrm{e}^{\mathbf{J}\tilde{\theta}}\,\boldsymbol{\Lambda}_{dq}(\mathrm{e}^{-\mathbf{J}\tilde{\theta}}\,\boldsymbol{i}_{\hat{d}q}) = \mathrm{e}^{\mathbf{J}\tilde{\theta}}\,\boldsymbol{L}(\boldsymbol{i}_{dq})\,\mathrm{e}^{-\mathbf{J}\tilde{\theta}} \cdot \boldsymbol{i}_{\hat{d}q} \qquad (3)$$

where $\boldsymbol{L}$ is the apparent inductance diagonal matrix with the d-axis L_d and the q-axis L_q. In sensorless schemes, the current model inductance $\boldsymbol{L}^i$ is computed in the estimated reference frame as

$$\boldsymbol{L}^i(\boldsymbol{i}_{\hat{d}q}) \cdot \boldsymbol{i}_{\hat{d}q} = \boldsymbol{\Lambda}_{dq}(\boldsymbol{i}_{\hat{d}q}). \qquad (4)$$

To formulate the relation of current model $\boldsymbol{L}^i(\boldsymbol{i}_{\hat{d}q})$ to the real inductance $\boldsymbol{L}(\boldsymbol{i}_{dq})$, the expression (4) is written as

$$\boldsymbol{L}^i(\boldsymbol{i}_{\hat{d}q}) \cdot \mathrm{e}^{\mathbf{J}\tilde{\theta}}\boldsymbol{i}_{dq} = \boldsymbol{\Lambda}_{dq}(\mathrm{e}^{\mathbf{J}\tilde{\theta}}\boldsymbol{i}_{dq}). \qquad (5)$$

Linearizing for small position error around the operating point marked by subscript 0 leads to

$$\boldsymbol{L}^i \cdot (\boldsymbol{i}_{dq} + \tilde{\theta}\,\mathbf{J}\,\boldsymbol{i}_{dq}) = \boldsymbol{\Lambda}_{dq}(\boldsymbol{i}_{dq0}) + \frac{\partial \boldsymbol{\Lambda}_{dq}}{\partial \boldsymbol{i}_{dq}}\,\tilde{\theta}\,\mathbf{J}\,\boldsymbol{i}_{dq0}. \qquad (6)$$

The incremental inductance matrix $\boldsymbol{L}_\partial$ is defined as

$$\boldsymbol{L}_\partial = \frac{\partial \boldsymbol{\lambda}_{dq}}{\partial \boldsymbol{i}_{dq}} = \begin{bmatrix} l_d & l_{dq} \\ l_{dq} & l_q \end{bmatrix} \qquad (7)$$

where l_d, l_q represents the incremental inductance along direct d and quadrature q axis, respectively, while l_{dq} is the cross-saturation term. All quantities are functions of $\boldsymbol{i}_{dq}$. On simplifying, the inductance model accounting position error (IMAP) is obtained as

$$\boldsymbol{L} \approx \boldsymbol{L}^i + \tilde{\theta}\,(\boldsymbol{L}^i - \boldsymbol{L}_\partial)\,\mathbf{J}. \qquad (8)$$
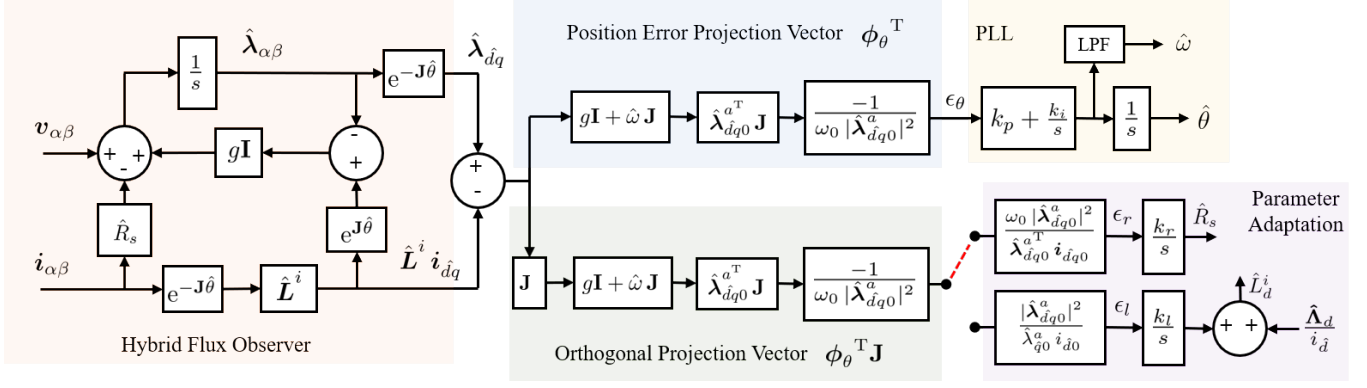
Fig. 3. Hybrid flux observer in stator reference frame with the APP position observer augmented with stator resistance and inductance adaptation.

IMAP is introduced in [15] as improved inductance model. The incremental inductance matrix $\boldsymbol{L}_\partial$ is computed in real-time from the flux map; as an example:

$$l_d(\boldsymbol{i}_{\hat{d}q}) = \frac{\boldsymbol{\Lambda}_{dq}(i_{\hat{d}} + \delta i_d, i_{\hat{q}}) - \boldsymbol{\Lambda}_{dq}(i_{\hat{d}}, i_{\hat{q}})}{\delta i_d} \quad (9)$$

where δi_d is a small value (≈ 10 mA). The other incremental inductances are computed in a similar fashion.

Let $\hat{\boldsymbol{\Lambda}}_{dq}$ denote the flux map LUTs accounting for parameter error. Then, the current model inductance is given by

$$\hat{\boldsymbol{L}}^i = \boldsymbol{L}^i - \tilde{\boldsymbol{L}} \quad (10)$$

where $\tilde{\boldsymbol{L}}$ is the inductance error matrix with components $\tilde{L}_d$ and $\tilde{L}_q$.

C. Hybrid Flux Observer

The hybrid flux observer (HFO) in stator reference frame is defined as

$$s\hat{\boldsymbol{\lambda}}_{\alpha\beta} = \boldsymbol{v}_{\alpha\beta} - \hat{R}_s \boldsymbol{i}_{\alpha\beta} + \boldsymbol{G}_{\alpha\beta}\left(\mathrm{e}^{\mathbf{J}\hat{\theta}}\hat{\boldsymbol{L}}^i \mathrm{e}^{-\mathbf{J}\hat{\theta}}\boldsymbol{i}_{\alpha\beta} - \hat{\boldsymbol{\lambda}}_{\alpha\beta}\right) \quad (11)$$

where $\boldsymbol{G}_{\alpha\beta}$ is a 2×2 gain matrix. The estimated stator resistance is denoted by $\hat{R}_s = R_s - \tilde{R}_s$ where $\tilde{R}_s$ is the resistance error. The flux observer is transformed to estimated rotor reference as

$$s\hat{\boldsymbol{\lambda}}_{\hat{d}q} = \boldsymbol{v}_{\hat{d}q} - \hat{R}_s \boldsymbol{i}_{\hat{d}q} - \hat{\omega}\mathbf{J}\hat{\boldsymbol{\lambda}}_{\hat{d}q} + \boldsymbol{G}\left(\hat{\boldsymbol{L}}^i \boldsymbol{i}_{\hat{d}q} - \hat{\boldsymbol{\lambda}}_{\hat{d}q}\right) \quad (12)$$

where the gain matrix $\boldsymbol{G}$ equivalence is given by

$$\boldsymbol{G} = \mathrm{e}^{-\mathbf{J}\hat{\theta}}\boldsymbol{G}_{\alpha\beta}\,\mathrm{e}^{\mathbf{J}\hat{\theta}}. \quad (13)$$

In this work, a diagonal matrix $\boldsymbol{G} = g\,\mathbf{I}$ is used where g can be inferred as a cross-over frequency between the current model at low speeds and voltage model at high speeds; hence, the equivalence $\boldsymbol{G} = \boldsymbol{G}_{\alpha\beta}$ holds.

D. Linearized Error Dynamics and Auxiliary Flux Definition

The non-linear flux estimation error dynamics [15] is derived from (12) as

$$s\tilde{\boldsymbol{\lambda}}_{\hat{d}q} = -(\boldsymbol{G} + \omega\mathbf{J})\tilde{\boldsymbol{\lambda}}_{\hat{d}q} + \boldsymbol{G}\left(\boldsymbol{\lambda}_{\hat{d}q} - \hat{\boldsymbol{L}}^i \boldsymbol{i}_{\hat{d}q} - \tilde{R}_s \boldsymbol{i}_{\hat{d}q}\right) \quad (14)$$

where the flux estimation error is $\tilde{\boldsymbol{\lambda}}_{\hat{d}q} = \boldsymbol{\lambda}_{\hat{d}q} - \hat{\boldsymbol{\lambda}}_{\hat{d}q}$. Linearizing around an operating point signified by a subscript 0 and using IMAP, the error dynamics simplifies to

$$\tilde{\boldsymbol{\lambda}}_{\hat{d}q} = (s\mathbf{I} + \boldsymbol{G} + \omega_0\mathbf{J})^{-1}\left(\boldsymbol{G}\left(\tilde{\theta}\,\hat{\boldsymbol{\lambda}}_{\hat{d}q0}^a + \tilde{\boldsymbol{L}}\,\boldsymbol{i}_{\hat{d}q0}\right) - \tilde{R}_s\boldsymbol{i}_{\hat{d}q0}\right) \quad (15)$$

where $\hat{\boldsymbol{\lambda}}_{\hat{d}q0}^a$ is the auxiliary flux linkage vector defined as

$$\hat{\boldsymbol{\lambda}}_{\hat{d}q0}^a = \left(\mathbf{J}\hat{\boldsymbol{L}}^i - \boldsymbol{L}_\partial\mathbf{J}\right)\boldsymbol{i}_{\hat{d}q0}. \quad (16)$$

E. MTPA Law in function of Auxiliary Flux Vector

The analytical expression for the MTPA law [19] is derived by differentiating torque w.r.t current angle γ as

$$\left.\frac{\mathrm{d}T}{\mathrm{d}\gamma}\right|_{|\boldsymbol{i}_{dq}|} = 0. \quad (17)$$

The terms relate to the real rotor reference frame (dq). Following (2),

$$\left(\frac{\mathrm{d}\boldsymbol{i}_{dq}}{\mathrm{d}\gamma}\right)^{\mathrm{T}}\mathbf{J}\boldsymbol{\lambda}_{dq} + \boldsymbol{i}_{dq}^{\mathrm{T}}\mathbf{J}\frac{\mathrm{d}\boldsymbol{\lambda}_{dq}}{\mathrm{d}\gamma} = 0. \quad (18)$$

Upon simplification and using the definition in (16),

$$\boldsymbol{i}_{dq}^{\mathrm{T}}\mathbf{J}\left(\mathbf{J}\boldsymbol{L} - \boldsymbol{L}_\partial\mathbf{J}\right)\boldsymbol{i}_{dq} = 0 \quad (19a)$$

$$\implies \boldsymbol{i}_{dq}^{\mathrm{T}}\mathbf{J}\boldsymbol{\lambda}_{dq}^a = 0. \quad (19b)$$

The expression (19b) dictates that the MTPA criterion is respected *if and only if* the stator current is in phase with the auxiliary flux vector.

III. PROPOSED SENSORLESS TECHNIQUE

The block diagram of sensorless scheme with flux observer, position estimation and parameter adaptation is shown in Fig. 3.

A. Speed and Position Tracking

The position error signal ϵ_θ is part of the general error signal ϵ obtained by manipulation of the observed and current model flux linkages from the HFO, as illustrated in Fig. 1.

Dealing with position tracking, a conventional phase lock loop (PLL) with a proportional-integral (PI) controller is employed to drive the position error signal ϵ_θ to zero as

$$\hat{\omega} = k_p\,\epsilon_\theta + \omega_i \qquad \omega_i = \int k_i\,\epsilon_\theta\,\mathrm{d}t \qquad \hat{\theta} = \int \hat{\omega}\,\mathrm{d}t \quad (20)$$

where k_p and k_i are the respective gains. The position error signal ϵ_θ is defined in the next section. The gains of the PLL are tuned for a critically damped response considering $\epsilon_\theta = \tilde{\theta}$ by placing the two poles at $s = -\Omega_\omega$ as

$$k_p = 2\,\Omega_\omega \qquad k_i = \Omega_\omega^2. \quad (21)$$

B. Projection Vector Framework

The general error signal ϵ is defined as the projection of difference in observed and current model flux estimates on a generic projection vector ϕ [5] [15], formulated as

$$\epsilon = \phi^{\mathrm{T}}\,(\hat{\boldsymbol{\lambda}}_{\hat{d}q} - \hat{\boldsymbol{L}}^{\,i}\,\boldsymbol{i}_{\hat{d}q}). \quad (22)$$

Following the results of flux error dynamics, the linearized form of the error signal is

$$\epsilon = \phi^{\mathrm{T}}\,(\hat{\boldsymbol{\lambda}}^{a}_{\hat{d}q0}\,\tilde{\theta} + \tilde{\boldsymbol{L}}\,\boldsymbol{i}_{\hat{d}q0} - \tilde{\boldsymbol{\lambda}}_{\hat{d}q}). \quad (23)$$

Using (15), the error signal (23) is expressed in terms of both position and parameter errors as

$$\epsilon = \phi^{\mathrm{T}}\,(s\mathbf{I} + \boldsymbol{G} + \omega_0\mathbf{J})^{-1}\cdot$$
$$\left((s\mathbf{I} + \omega_0\mathbf{J})(\hat{\boldsymbol{\lambda}}^{a}_{\hat{d}q0}\,\tilde{\theta} + \tilde{\boldsymbol{L}}\,\boldsymbol{i}_{\hat{d}q0}) + \tilde{R}_s\,\boldsymbol{i}_{\hat{d}q0}\right). \quad (24)$$

Decomposing (24) in terms of constituent errors, the error signal is expressed as

$$\epsilon = \phi^{\mathrm{T}} \begin{bmatrix} \boldsymbol{h}_{\tilde{\theta}} & \boldsymbol{h}_{\tilde{L}_d} & \boldsymbol{h}_{\tilde{L}_q} & \boldsymbol{h}_{\tilde{R}_s} \end{bmatrix} \tilde{\boldsymbol{x}} \quad (25a)$$

$$\boldsymbol{h}_{\tilde{\theta}} = (s\mathbf{I} + \boldsymbol{G} + \omega_0\mathbf{J})^{-1}(s\mathbf{I} + \omega_0\mathbf{J})\,\hat{\boldsymbol{\lambda}}^{a}_{\hat{d}q0}$$
$$\boldsymbol{h}_{\tilde{L}_d} = (s\mathbf{I} + \boldsymbol{G} + \omega_0\mathbf{J})^{-1}(s\mathbf{I} + \omega_0\mathbf{J})\begin{bmatrix} i_{\hat{d}0} & 0 \end{bmatrix}^{\mathrm{T}}$$
$$\boldsymbol{h}_{\tilde{L}_q} = (s\mathbf{I} + \boldsymbol{G} + \omega_0\mathbf{J})^{-1}(s\mathbf{I} + \omega_0\mathbf{J})\begin{bmatrix} 0 & i_{\hat{q}0} \end{bmatrix}^{\mathrm{T}}$$
$$\boldsymbol{h}_{\tilde{R}_s} = (s\mathbf{I} + \boldsymbol{G} + \omega_0\mathbf{J})^{-1}\,\boldsymbol{i}_{\hat{d}q0} \quad (25b)$$

where $\tilde{\boldsymbol{x}} = \begin{bmatrix} \tilde{\theta} & \tilde{L}_d & \tilde{L}_q & \tilde{R}_s \end{bmatrix}^{\mathrm{T}}$ and the operators $\boldsymbol{h}$ are 2×1 vectors.

As an example, let ϕ_θ be the position error projection vector and ϵ_θ the position error signal. Then, the steady-state position error $\tilde{\theta}_0$ owing to parametric errors can be derived by equating $\epsilon_\theta = 0$ as

$$\tilde{\theta}_0 = -\left.\frac{\phi_\theta^{\mathrm{T}}\left(\boldsymbol{h}_{\tilde{L}_d}\,\tilde{L}_d + \boldsymbol{h}_{\tilde{L}_q}\,\tilde{L}_q + \boldsymbol{h}_{\tilde{R}_s}\,\tilde{R}_s\right)}{\phi_\theta^{\mathrm{T}}\,\boldsymbol{h}_{\tilde{\theta}}}\right|_{s=0}. \quad (26)$$

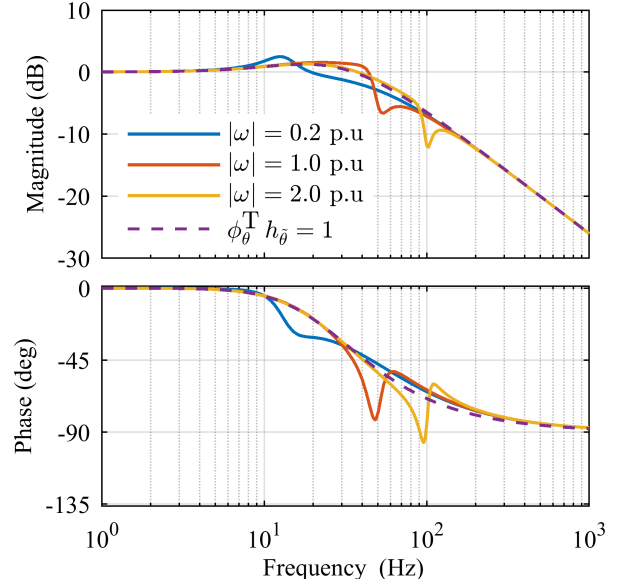Steady-state error in the case of parameter adaptation can be derived in a similar fashion.

Fig. 4. Frequency response of closed loop position observer [1] for simplified projection vector (28) at three different operating speeds; dotted lines correspond to the ideal projection vector with derivative term (27). Parameters: $g = 2\pi \cdot 10$ rad/s, $\Omega_\omega = 2\pi \cdot 25$ rad/s.

In conclusion, the generic error signal ϵ is a function of position and parameter errors. Due to the 2-dimensional nature of the error space (dq), only two errors out of four can be compensated concurrently.

C. Adaptive Projection Vector for Position Error Estimation

The position error projection vector ϕ_θ is designed to hold the equality between position error signal and position error, $\epsilon_\theta = \tilde{\theta}$, in the absence of parametric errors, i.e., $\phi_\theta^{\mathrm{T}}\,\boldsymbol{h}_{\tilde{\theta}} = 1$. From (25), this leads to a projection vector of nature:

$$\phi_\theta^{\mathrm{T}} = \frac{-1}{\omega_0\,|\hat{\boldsymbol{\lambda}}^{a}_{\hat{d}q0}|^2}\,\hat{\boldsymbol{\lambda}}^{a\mathrm{T}}_{\hat{d}q0}\,\mathbf{J}\,(s\,\mathbf{I} + \boldsymbol{G} + \omega_0\,\mathbf{J}). \quad (27)$$

It has been shown in [1] that the derivative term $s\mathbf{I}$ is non-essential as far as the position error is concerned. Hence the adaptive projection vector for position error estimation is derived by dropping the derivative term as

$$\phi_\theta^{\mathrm{T}} = \frac{-1}{\omega_0\,|\hat{\boldsymbol{\lambda}}^{a}_{\hat{d}q0}|^2}\,\hat{\boldsymbol{\lambda}}^{a\mathrm{T}}_{\hat{d}q0}\,\mathbf{J}\,(\boldsymbol{G} + \omega_0\,\mathbf{J}). \quad (28)$$

To further support the simplification, frequency response of the closed loop position observer is analyzed. For the PLL of structure (20), the closed loop transfer function is given by

$$\frac{\hat{\theta}(s)}{\theta(s)} = \frac{(sk_p + k_i)\,\phi_\theta^{\mathrm{T}}\,\boldsymbol{h}_{\tilde{\theta}}}{s^2 + (sk_p + k_i)\,\phi_\theta^{\mathrm{T}}\,\boldsymbol{h}_{\tilde{\theta}}} \quad (29)$$

where the transfer function between the position error signal and position error is

$$\phi_\theta^{\mathrm{T}}\,\boldsymbol{h}_{\tilde{\theta}} = \frac{\epsilon_\theta}{\tilde{\theta}} = \frac{s^2 + sg + g^2 + \omega_0^2}{(s + g)^2 + \omega_0^2}. \quad (30)$$

It can be inferred that the transfer function is independent of the operating point $\boldsymbol{i}_{\hat{d}q}$ and the sign of rotation.
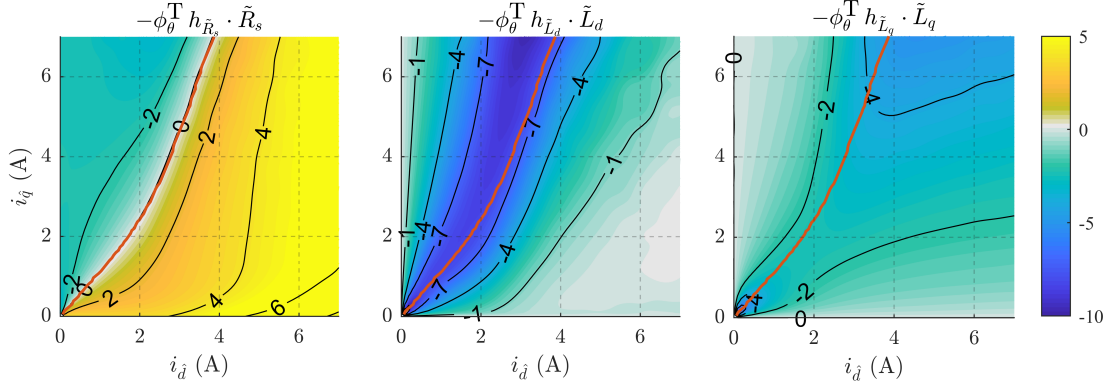
Fig. 5. Steady-state position error $\tilde{\theta}_0$ in ° (electrical) of APP based position observer due to parameter inaccuracies: (a) $\tilde{R}_s = 0.25\,R_s$ at $\omega = 2\,\pi \cdot 10$ rad/s; (b) $\tilde{L}_d = 0.25\,L_d$; (c) $\tilde{L}_q = 0.25\,L_q$.

Fig. 4 shows the frequency response plot of (29) at different operating speeds for the simplified projection vector (28) and the ideal projection vector with derivative term (27). Notice that the closed loop bandwidth is only marginally altered by the absence of derivative term; hence, the simplification is reasonable.

D. Resistance Immunity of APP

The sensitivity of proposed position error projection vector (28) to resistance error is drawn from the steady-state position error expression (26) at $\tilde{L}_d = \tilde{L}_q = 0$ as

$$\tilde{\theta}_0 = -\tilde{R}_s \cdot \left.\frac{\boldsymbol{\phi}_\theta^{\mathrm{T}}\,\boldsymbol{h}_{\tilde{R}_s}}{\boldsymbol{\phi}_\theta^{\mathrm{T}}\,\boldsymbol{h}_{\tilde{\theta}}}\right|_{s=0} = \frac{\tilde{R}_s}{\omega_0\,|\hat{\boldsymbol{\lambda}}_{\hat{d}q0}^a|^2}\,\hat{\boldsymbol{\lambda}}_{\hat{d}q0}^{a^{\mathrm{T}}}\,\mathbf{J}\,\boldsymbol{i}_{\hat{d}q0}. \quad (31)$$

The term $\hat{\boldsymbol{\lambda}}_{\hat{d}q0}^{a^{\mathrm{T}}}\,\mathbf{J}\,\boldsymbol{i}_{\hat{d}q0}$ in (31) is the MTPA law derived in (19b). This implies that the chosen projection vector (28) is immune to resistance error on MTPA trajectory.

Fig. 5(a) shows the contour of steady-state position error (31) for a 25% error in resistance, $\tilde{R}_s = 0.25\,R_s$, at an operating speed of $\omega = 2\,\pi \cdot 10$ rad/s. The position error $\tilde{\theta}_0$ is seen to diminish towards the MTPA trajectory. As $\tilde{\theta}_0$ in (31) is inversely proportional to ω, the $\tilde{R}_s$ becomes less relevant at higher speeds, expectedly.

It is worth mentioning that the fundamental component of the voltage error arising due to inverter dead-time is in phase with the stator current vector $\boldsymbol{i}_{\hat{d}q}$ and is reflected in the resistive error term $\tilde{R}_s$. Consequently, immunity also extends towards non-ideal compensation of inverter errors. This is demonstrated experimentally in later section.

E. Susceptibility to Inductance Errors

The sensitivity of APP to inductance errors $\tilde{L}_d$ and $\tilde{L}_q$ are analyzed by evaluating the steady-state position error in (32) and (33), respectively.

$$\tilde{\theta}_0 = -\tilde{L}_d \cdot \left.\frac{\boldsymbol{\phi}_\theta^{\mathrm{T}}\,\boldsymbol{h}_{\tilde{L}_d}}{\boldsymbol{\phi}_\theta^{\mathrm{T}}\,\boldsymbol{h}_{\tilde{\theta}}}\right|_{s=0} = -\tilde{L}_d\,\frac{\hat{\lambda}_{\hat{d}0}^a\,i_{\hat{d}0}}{|\hat{\boldsymbol{\lambda}}_{\hat{d}q0}^a|^2} \quad (32)$$

$$\tilde{\theta}_0 = -\tilde{L}_q \cdot \left.\frac{\boldsymbol{\phi}_\theta^{\mathrm{T}}\,\boldsymbol{h}_{\tilde{L}_q}}{\boldsymbol{\phi}_\theta^{\mathrm{T}}\,\boldsymbol{h}_{\tilde{\theta}}}\right|_{s=0} = -\tilde{L}_q\,\frac{\hat{\lambda}_{\hat{q}0}^a\,i_{\hat{q}0}}{|\hat{\boldsymbol{\lambda}}_{\hat{d}q0}^a|^2}. \quad (33)$$

Fig. 5(b) & 5(c) plots the contour of steady-state position error for a 25% inductance error, i.e., $\tilde{L}_d = 0.25\,L_d$ and $\tilde{L}_q = 0.25\,L_q$, respectively. It is observed in Fig. 5(b) that regions in the vicinity of MTPA trajectory are particularly sensitive to $\tilde{L}_d$, resulting in steady-state position error as high as $\approx 10°$. APP is relatively less sensitive to $\tilde{L}_q$ as shown in Fig. 5(c) where the maximum position error is $\approx 5°$ at high loads. Contrary to the resistance error, the influence of inductance error is speed independent.

IV. PARAMETER ADAPTATION

Exploiting the two degrees of freedom of the error domain, a second projection vector $(\boldsymbol{\phi}_\theta^{\mathrm{T}}\,\mathbf{J})$ orthogonal to APP can be utilized to adapt parameters for improved reliability. To this end, an generic error signal ϵ_j for parameter adaptation is defined as

$$\begin{aligned}\epsilon_j &= \boldsymbol{\phi}_\theta^{\mathrm{T}}\,\mathbf{J}\,(\hat{\boldsymbol{\lambda}}_{\hat{d}q} - \hat{\boldsymbol{L}}^i\,\boldsymbol{i}_{\hat{d}q}) \\ &= \boldsymbol{\phi}_\theta^{\mathrm{T}}\,\mathbf{J}\,\begin{bmatrix}\boldsymbol{h}_{\tilde{\theta}} & \boldsymbol{h}_{\tilde{L}_d} & \boldsymbol{h}_{\tilde{L}_q} & \boldsymbol{h}_{\tilde{R}_s}\end{bmatrix}\,\tilde{\boldsymbol{x}}.\end{aligned} \quad (34)$$

Owing to the orthogonality, the position error does not influence the adaptation error signal ϵ_j in steady-state, i.e.,

$$\boldsymbol{\phi}_\theta^{\mathrm{T}}\,\mathbf{J}\,\boldsymbol{h}_{\tilde{\theta}}|_{s=0} = 0. \quad (35)$$

Among the three parameter errors $(\tilde{L}_d,\ \tilde{L}_q,\ \tilde{R}_s)$ in contention, the feasibility of adaptation is determined by evaluating the steady-state coefficients (DC gain) of error signal ϵ_j in (25), reported in the following expressions:

$$\boldsymbol{\phi}_\theta^{\mathrm{T}}\,\mathbf{J}\,\boldsymbol{h}_{\tilde{L}_d}|_{s=0} = \frac{1}{|\hat{\boldsymbol{\lambda}}_{\hat{d}q0}^a|^2}\,\hat{\lambda}_{\hat{q}0}^a\,i_{\hat{d}0} \quad (36)$$

$$\boldsymbol{\phi}_\theta^{\mathrm{T}}\,\mathbf{J}\,\boldsymbol{h}_{\tilde{L}_q}|_{s=0} = \frac{-1}{|\hat{\boldsymbol{\lambda}}_{\hat{d}q0}^a|^2}\,\hat{\lambda}_{\hat{d}0}^a\,i_{\hat{q}0} \quad (37)$$

$$\boldsymbol{\phi}_\theta^{\mathrm{T}}\,\mathbf{J}\,\boldsymbol{h}_{\tilde{R}_s}|_{s=0} = \frac{1}{\omega_0\,|\hat{\boldsymbol{\lambda}}_{\hat{d}q0}^a|^2}\,\hat{\boldsymbol{\lambda}}_{\hat{d}q0}^{a^{\mathrm{T}}}\,\boldsymbol{i}_{\hat{d}q0}. \quad (38)$$
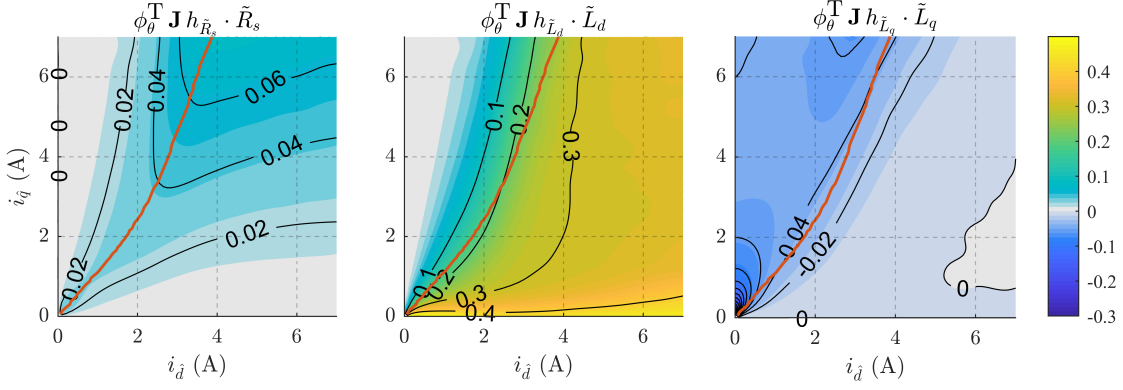
Fig. 6. Steady-state error signal ϵ_j of orthogonal to APP projection vector $\phi_\theta^{\mathrm{T}} \mathbf{J}$ due to parameter inaccuracies: (a) $\tilde{R}_s = 0.25\,R_s$ at $\omega = 2\,\pi \cdot 10$ rad/s; (b) $\tilde{L}_d = 0.25\,L_d$; (c) $\tilde{L}_q = 0.25\,L_q$. Note that the error signal ϵ_j is dimensionless.

A sufficiently high DC gain is essential for reliable adaptation; bigger the gain, better is the prospect for adaptation. For a fair comparison, the magnitude of error signal ϵ_j is calculated for a 25% parametric error in $\tilde{R}_s = 0.25\,R_s$, $\tilde{L}_d = 0.25\,L_d$ and $\tilde{L}_q = 0.25\,L_q$, shown in Fig. 6(a), 6(b) and 6(c) respectively. The d-axis inductance error is seen to noticeably dominant by a factor of ≈ 4, indicating a strong prospect for $\tilde{L}_d$ adaptation.

A. Stator Resistance Adaptation

In presence of accurate flux-map LUTs, a stator resistance adaptation can be resorted to track temperature induced variations. The APP technique is inherently immune to $\tilde{R}_s$ and dead-time on MTPA trajectory as pointed out in preceding section. However, high performance drives can benefit from accurate flux and torque estimation that are susceptible to resistance error.

The resistance error signal ϵ_r is defined in (39) where ϕ_r is the resistance error projection vector.

$$\epsilon_r = \phi_r^{\mathrm{T}} (\hat{\boldsymbol{\lambda}}_{\hat{d}q} - \hat{\boldsymbol{L}}^i \boldsymbol{i}_{\hat{d}q}). \tag{39}$$

Akin to the design of APP, the resistance error projection vector ϕ_r is desired to hold the equality between resistance error signal and resistance error, $\epsilon_r = \tilde{R}_s$, in steady-state. It follows from (38) that ϕ_r should be of nature:

$$\phi_r^{\mathrm{T}} = \frac{\omega_0 |\hat{\boldsymbol{\lambda}}_{\hat{d}q0}^a|^2}{\hat{\boldsymbol{\lambda}}_{\hat{d}q0}^{a\mathrm{T}} \boldsymbol{i}_{\hat{d}q0}} \phi_\theta^{\mathrm{T}} \mathbf{J}. \tag{40}$$

A resistance adaption law is defined with gain k_r as

$$\hat{R}_s = k_r \int \epsilon_r \, \mathrm{d}t. \tag{41}$$

As alluded to earlier, the fundamental component of voltage error due to non-ideal dead-time compensation is along the current vector. Thus, the adapted resistance will be

$$\hat{R}_s = R_s + \frac{1}{|\boldsymbol{i}_{dq}|} \frac{4}{3} v_{dc} f_s \tilde{t}_d \tag{42}$$

where v_{dc} is the dc-link voltage, f_s is the switching frequency and $\tilde{t}_d = t_d - \hat{t}_d$ is the error in compensated dead-time.

The expression (42) suggests that the resistance estimation is more sensitive to dead-time error for small current magnitude. However, the voltage error due to dead-time is diminished at small currents due to parasitic capacitance [20]. Moreover, as depicted in Fig. 6(a), the error signal diminishes at small loads making it unobservable; hence, the resistance adaptation is disabled for $|T| < 0.2$ p.u.

For small loads, the control deviates from MTPA trajectory due to the necessary minimum excitation in d-axis. Thus, a conflicting situation arises: the resistance adaption is not feasible in the regions where APP is susceptible. The resulting steady-state position error is unavoidable, as predicted in Fig. 5(a). Adaptation is resumed at high loads which primarily benefits accurate stator flux and torque estimation. Moreover, it suffers from poor signal to noise ratio at high speeds and is disabled for $|\omega| > 0.75$ p.u.

B. Inductance Adaptation

In presence of inaccurate flux-maps LUT, adapting resistance is not advisable as the error signal ϵ_j due to d-axis inductance error in Fig. 6(b) is more dominant over resistance error in Fig. 6(a) and could result in potential instability. Hence, adaptation of $\tilde{L}_d$ is preferred which further helps to reduce the steady-state position error in Fig. 5(b).

The inductance error signal ϵ_l is defined as

$$\epsilon_l = \phi_l^{\mathrm{T}} (\hat{\boldsymbol{\lambda}}_{\hat{d}q} - \hat{\boldsymbol{L}}^i \boldsymbol{i}_{\hat{d}q}) \tag{43}$$

where ϕ_l is the inductance error projection vector. To satisfy the equality, $\epsilon_l = \tilde{L}_d$ in steady-state, it follows from (36) that the inductance error projection vector ϕ_l should be of nature

$$\phi_l^{\mathrm{T}} = \frac{|\hat{\boldsymbol{\lambda}}_{\hat{d}q0}^a|^2}{\hat{\lambda}_{\hat{q}0}^a i_{\hat{d}0}} \phi_\theta^{\mathrm{T}} \mathbf{J}. \tag{44}$$

The inductance adaptation law is defined with gain k_l as

$$\hat{L}_d^i = \frac{\hat{\boldsymbol{\Lambda}}_d(\boldsymbol{i}_{\hat{d}q})}{i_{\hat{d}}} + k_l \int \epsilon_l \, \mathrm{d}t. \tag{45}$$

The adaptation term is added to the current model inductance estimate for faster convergence. A small steady-state error $\tilde{L}_{d0}$
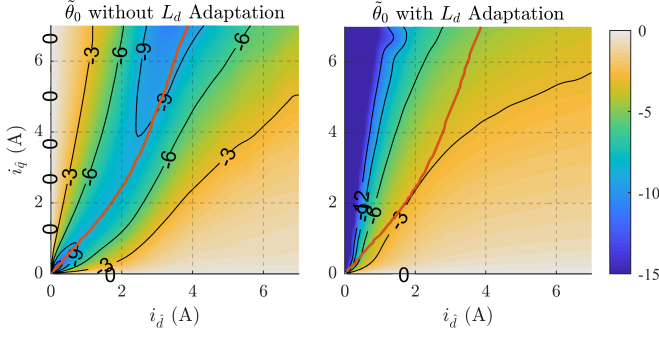
Fig. 7. Steady-state position error in ° (electrical) at $\tilde{L}_d = 0.2\,L_d$ and $\tilde{L}_q = 0.2\,L_q$: (a) Without inductance adaptation; (b) With inductance adaptation.
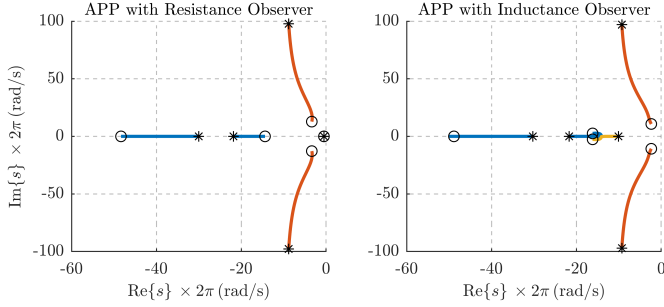

Fig. 8. Locus of poles for $\omega = 0.2 \ldots 2$ p.u at $T = 1$ p.u. where the markers $\circ$ and $*$ denote the speeds 0.2 and 2 p.u respectively: (a) Position and resistance observer; (b) Position and inductance observer. Color code: PLL poles are denoted in blue, flux observer in red, resistance/inductance observer in yellow.
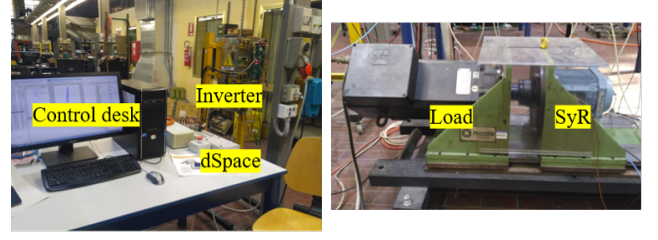

Fig. 9. Experimental Setup of 1.1 kW SyR motor under test on a dSPACE DS1103 control platform at a sampling frequency of 10 kHz.

TABLE I
MOTOR AND INVERTER PARAMETERS

Parameters	Symbol	Values	Units
Rated power	P_n	1.1	kW
Rated speed	ω_n	1500	rpm
Rated torque	T_n	7.1	Nm
Rated voltage	V_n	340	V
Rated current	I_n	2.3	A
Pole pairs	p	2	-
Stator resistance	R_s	4.5	Ω
Shaft inertia	J	0.04	kgm^2
DC-link voltage	v_{dc}	565	V
Nominal dead-time	t_d	1.9	μs

persists in the presence of q-axis flux-maps errors $(\tilde{L}_q)$, given by

$$\tilde{L}_{d0} = -\tilde{L}_q \cdot \left. \frac{\boldsymbol{\phi}_l^{\mathrm{T}}\, \boldsymbol{h}_{\tilde{L}_q}}{\boldsymbol{\phi}_l^{\mathrm{T}}\, \boldsymbol{h}_{\tilde{L}_d}} \right|_{s=0} = \tilde{L}_q \cdot \frac{\hat{\lambda}_{\hat{d}0}^a\, i_{\hat{q}0}}{\hat{\lambda}_{\hat{q}0}^a\, i_{\hat{d}0}}. \tag{46}$$

The resulting steady-state position error under inductance adaptation is derived from (32), (33) and (46) as

$$\tilde{\theta}_0 = \frac{-\tilde{L}_q}{|\hat{\boldsymbol{\lambda}}_{\hat{d}q0}^a|^2} \left(\hat{\lambda}_{\hat{q}0}^a i_{\hat{q}0} + \hat{\lambda}_{\hat{d}0}^a i_{\hat{d}0}\, \frac{\hat{\lambda}_{\hat{d}0}^a\, i_{\hat{q}0}}{\hat{\lambda}_{\hat{q}0}^a\, i_{\hat{d}0}} \right). \tag{47}$$

Fig. 7 shows the contour of position error with and without inductance adaptation at $\tilde{L}_d = 0.2\,L_d$, $\tilde{L}_q = 0.2\,L_q$; no resistance error is considered. A conspicuous improvement in position error along the MTPA trajectory is discerned, experimentally validated in the succeeding section.

A large position error is noticed in Fig. 7(b) for operating points away from MTPA trajectory towards the q-axis. The adaptation should be disabled at these operating points where the strength of $\tilde{L}_d$ signal gets progressively weaker (see Fig. 6(b)).

V. STABILITY ANALYSIS

The gains of PLL are chosen for a critically damped response (21) with the poles at $s = -\Omega_\omega = -2\,\pi \cdot 25$ rad/s, corresponds to a bandwidth of $2\,\pi \cdot 62$ rad/s. The flux observer gain is set to 0.2 p.u of rated speed as $g = 2\,\pi \cdot 10$ rad/s. Owing to slow time-varying nature, the resistance observer gain is set

to $k_r = 2\,\pi \cdot 0.5$ rad/s. The bandwidth of inductance observer is chosen to $k_l = 2\,\pi \cdot 10$ rad/s.

A. APP with Resistance Adaptation

The error dynamics of the position observer in (20) is be expressed as

$$s\,\tilde{\theta} = \tilde{\omega}_i - k_p\,\epsilon_\theta \qquad s\,\tilde{\omega}_i = -k_i\,\epsilon_\theta. \tag{48}$$

The combined dynamics of flux, position and resistance observers is given by

$$s\,\boldsymbol{y}_r = \boldsymbol{A}_r\,\boldsymbol{y}_r \tag{49}$$

$$\boldsymbol{A}_r = \begin{bmatrix} -(\boldsymbol{G}_0 + \omega_0\,\mathbf{J}) & \boldsymbol{G}_0\,\hat{\boldsymbol{\lambda}}_{\hat{d}q0}^a & \mathbf{0} & -\boldsymbol{i}_{\hat{d}q0} \\ k_p\,\boldsymbol{\phi}_\theta^{\mathrm{T}} & -k_p\,\boldsymbol{\phi}_\theta^{\mathrm{T}}\,\hat{\boldsymbol{\lambda}}_{\hat{d}q0}^a & 1 & 0 \\ k_i\,\boldsymbol{\phi}_\theta^{\mathrm{T}} & -k_i\,\boldsymbol{\phi}_\theta^{\mathrm{T}}\,\hat{\boldsymbol{\lambda}}_{\hat{d}q0}^a & 0 & 0 \\ k_r\,\boldsymbol{\phi}_r^{\mathrm{T}} & -k_r\,\boldsymbol{\phi}_r^{\mathrm{T}}\,\hat{\boldsymbol{\lambda}}_{\hat{d}q0}^a & 0 & 0 \end{bmatrix}$$

where $\boldsymbol{y}_r = \begin{bmatrix} \tilde{\boldsymbol{\lambda}}_{\hat{d}q} & \tilde{\theta} & \tilde{\omega}_i & \tilde{R}_s \end{bmatrix}^{\mathrm{T}}$. Fig. 8(a) shows the movement of poles for $\omega = 0.2 \ldots 2$ p.u. The poles are seen to converge to their designed value at high speeds; the movement of the resistance observer pole (yellow line), although dependent on operating point, is not as pronounced as the PLL and flux observer poles. Stability at $T = 1$ p.u is ascertained.

Note that the control system becomes unstable for large values of k_r (eg. $2\pi \cdot 10$ rad/s) at low speeds. Since temperature is slow time-varying, a high k_r is unwarranted.

B. APP with Inductance Adaptation

The combined dynamics of flux, position and inductance observer is expressed as

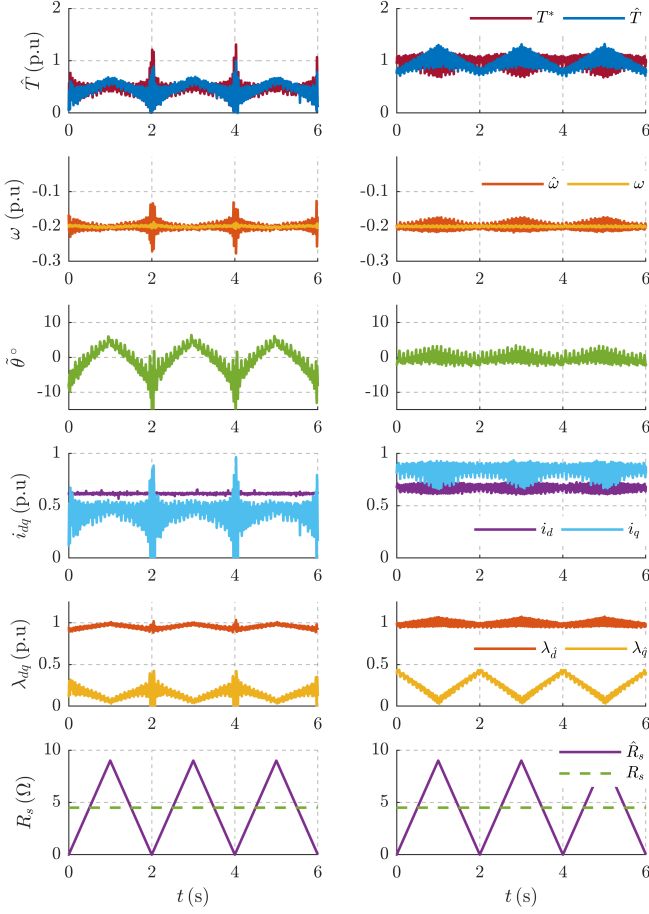$$s\boldsymbol{y}_l = \boldsymbol{A}_l\,\boldsymbol{y}_l \tag{50}$$

Fig. 10. Immunity of observed position in the APP technique to resistance variation of $\tilde{R}_s = \pm 1$ p.u ($\pm 4.5\Omega$) at $\omega = -0.2$ p.u: (a) $T_L = 0.5$ p.u, away from MTPA due to i_d^{min}; (b) $T_L = 1$ p.u, on MTPA trajectory.

Fig. 11. Variations on dead-time compensation ($\pm 1\mu s$) to emulate $\tilde{R}_s$ at $T_L = 0.5$ p.u and $\omega = -0.2$ p.u: (a) Without R_s adaptation; (b) With R_s adaptation.

$$
\boldsymbol{A}_l = \begin{bmatrix}
-(\boldsymbol{G} + \omega_0\,\mathbf{J}) & \boldsymbol{G}\,\hat{\boldsymbol{\lambda}}_{\hat{d}q0}^a & \mathbf{0} & \boldsymbol{G}\begin{bmatrix} i_{\hat{d}0} & 0 \end{bmatrix}^\mathsf{T} \\
k_p\,\boldsymbol{\phi}_\theta^\mathsf{T} & -k_p\,\boldsymbol{\phi}_\theta^\mathsf{T}\,\hat{\boldsymbol{\lambda}}_{\hat{d}q0}^a & 1 & -k_p\,\boldsymbol{\phi}_\theta^\mathsf{T}\begin{bmatrix} i_{\hat{d}0} & 0 \end{bmatrix}^\mathsf{T} \\
k_i\,\boldsymbol{\phi}_\theta^\mathsf{T} & -k_i\,\boldsymbol{\phi}_\theta^\mathsf{T}\,\hat{\boldsymbol{\lambda}}_{\hat{d}q0}^a & 0 & -k_i\,\boldsymbol{\phi}_\theta^\mathsf{T}\begin{bmatrix} i_{\hat{d}0} & 0 \end{bmatrix}^\mathsf{T} \\
k_l\,\boldsymbol{\phi}_l^\mathsf{T} & -k_l\,\boldsymbol{\phi}_l^\mathsf{T}\,\hat{\boldsymbol{\lambda}}_{\hat{d}q0}^a & 0 & -k_l\,\boldsymbol{\phi}_l^\mathsf{T}\begin{bmatrix} i_{\hat{d}0} & 0 \end{bmatrix}^\mathsf{T}
\end{bmatrix}
$$

where $\boldsymbol{y}_l = \begin{bmatrix} \tilde{\boldsymbol{\lambda}}_{\hat{d}q} & \tilde{\theta} & \tilde{\omega}_i & \tilde{L}_d \end{bmatrix}^\mathsf{T}$. Fig. 8(b) shows the movement of poles for $\omega = 0.2\ldots 2$ p.u at $T = 1$ p.u. Similar to the former case, the poles are seen to converge to their designated value at high speeds.

The migration of PLL and inductance observer poles is due to the absence of the derivative term in the simplified projection vector (28), making it operating point dependent. Nevertheless, stability is ascertained.

VI. EXPERIMENTAL RESULTS

The proposed sensorless scheme is validated experimentally with a 1.1 kW SyR motor on a dSPACE DS1103 control platform at a sampling frequency of 10 kHz. The output of PLL is low pass filtered at Ω_ω. A PI speed controller with critically damped poles at $s = -2\pi \cdot 1$ rad/s is used for close loop control. Load torque is imposed by the auxiliary drive connected to the shaft. The parameters of the SyR motor under test are tabulated in Table I.
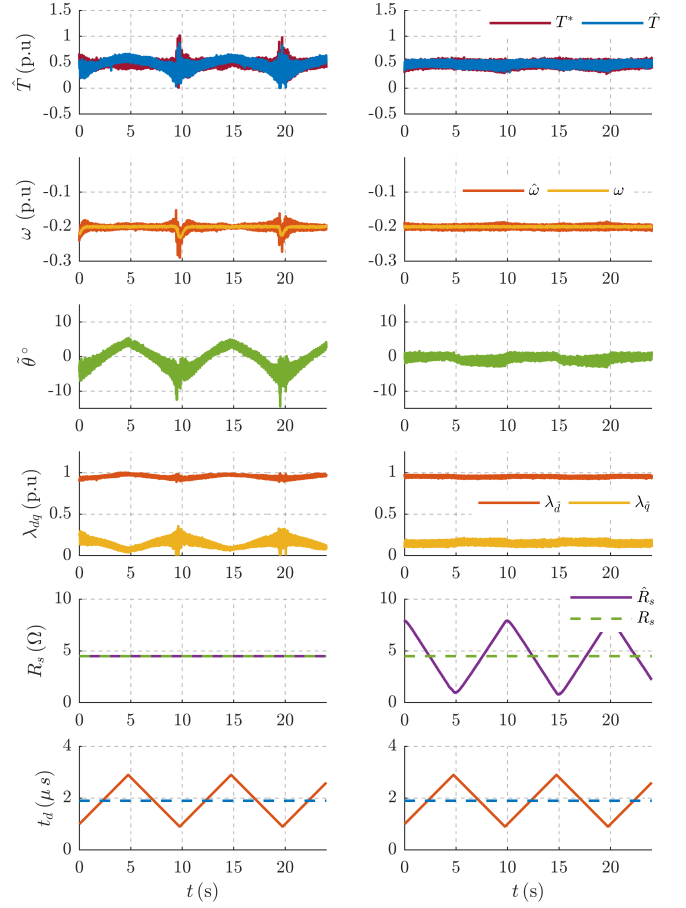
Note that a high minimum current in $i_d^{min} = 0.6$ p.u (2A) is intentionally imposed to move the operation away from MTPA to facilitate the demonstration of susceptibility of APP to resistance error and the effectiveness of resistance adaptation in mitigation.

A. Immuntity of Proposed APP to $\tilde{R}_s$

The immunity of proposed technique to resistance variation on MTPA trajectory is demonstrated in this section. A perturbation of $\pm 100\%$ is injected to resistance within the control, $\hat{R}_s$, with the physical stator resistance R_s remaining constant. A load torque of $T_L = 0.5$ p.u (non-MTPA) and $T_L = 1$ p.u (MTPA) is imposed in Fig 10(a) and 10(b), respectively. Despite the variations in observed flux and torque in Fig. 10(b), the position is undeterred. However, when the MTPA is not respected as in Fig. 10(a), the observed position is susceptible to $\tilde{R}_s$. In either scenario, stability is not compromised.

B. Stator Resistance Adaptation

The competency of resistance adaption is studied by imposing deliberate variations on the dead-time compensation which is equivalent to physical variations in resistance. A dead-time variation of $\tilde{t}_d = \pm 1\mu s$ is equivalent to $\pm 3\ \Omega$ at $T_L = 0.5$ p.u;
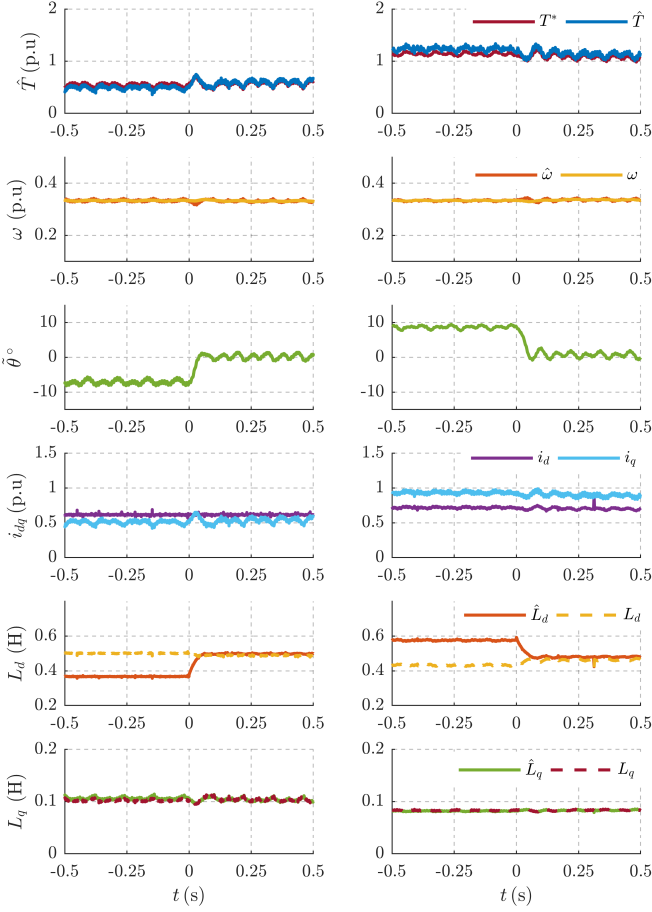
Fig. 12. Validation of d-axis inductance adaptation, enabled at $t = 0$ s: (a) +25% error $\hat{\mathbf{\Lambda}}_d = 0.75\,\mathbf{\Lambda}_d$ at $T_L = 0.5$ p.u; (b) -25% error $\hat{\mathbf{\Lambda}}_d = 1.25\,\mathbf{\Lambda}_d$ at $T_L = 1$ p.u..
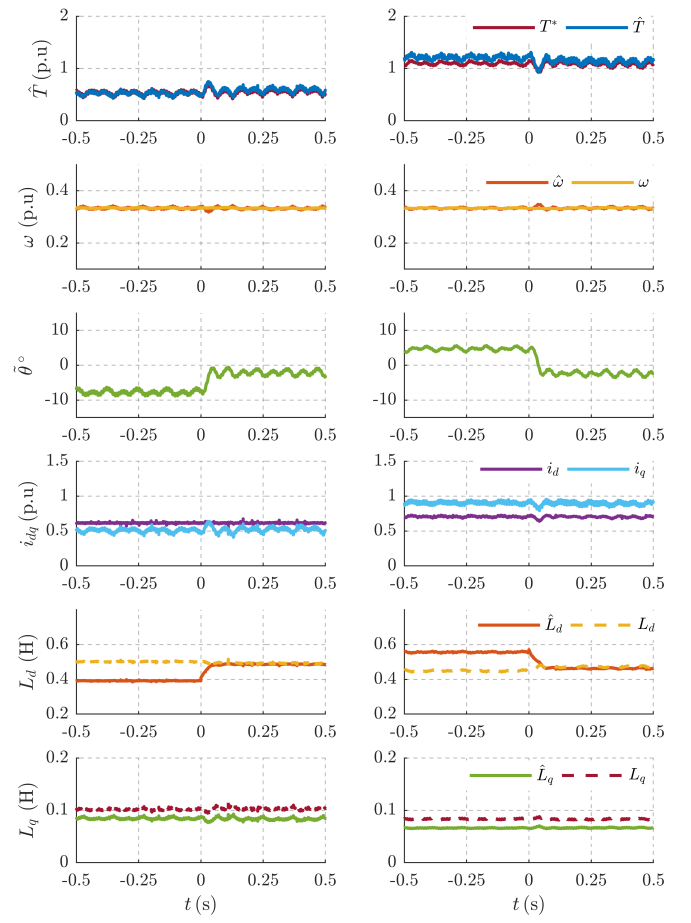
Fig. 13. Validation of d-axis inductance adaptation at $\hat{\mathbf{\Lambda}}_q = 0.75\,\mathbf{\Lambda}_q$, enabled at $t = 0$ s: (a) +25% error $\hat{\mathbf{\Lambda}}_d = 0.75\,\mathbf{\Lambda}_d$ at $T_L = 0.5$ p.u; (b) -25% error $\hat{\mathbf{\Lambda}}_d = 1.25\,\mathbf{\Lambda}_d$ at $T_L = 1$ p.u.

the equivalence is a function of peak current and changes with load as expressed in (42). In Fig. 11(a) and 11(b), the effect of changes in dead-time without and with resistance adaption is shown in juxtaposition. With the adaptation, the $\hat{R}_s$ tracks the changes in dead-time and thereby alleviates the impact on the observed position, the stator flux and the torque.

C. Inductance Adaptation

A series of tests are conducted to validate the proposed inductance adaptation scheme. In Fig. 12(a), a +25% error in d-axis flux-maps LUT ($\hat{\mathbf{\Lambda}}_d = 0.75\,\mathbf{\Lambda}_d$) is imposed at $T_L = 0.5$ p.u while in Fig. 12(b), a -25% error ($\hat{\mathbf{\Lambda}}_d = 1.25\,\mathbf{\Lambda}_d$) is imposed at $T_L = 1$ p.u. Accurate q-axis flux-maps is considered. For $t < 0$ s without adaptation, the steady-state position error owing to $\tilde{L}_d$ is $\approx 9°$ (electrical). The inductance adaptation is enabled at time $t = 0$ s upon which the position error reduces to zero as estimated $\hat{L}_d^i$ converges to L_d.

The performance under parametric error in both d and q-axes flux-maps is analyzed in Fig. 13. An error of +20 % is imposed ($\hat{\mathbf{\Lambda}}_d = 0.8\,\mathbf{\Lambda}_d$ and $\hat{\mathbf{\Lambda}}_q = 0.8\,\mathbf{\Lambda}_q$) at $T_L = 0.5$ p.u in Fig. 13(a) while an error of -20% in d and +20 in q ($\hat{\mathbf{\Lambda}}_d = 1.2\,\mathbf{\Lambda}_d$ and $\hat{\mathbf{\Lambda}}_q = 0.8\,\mathbf{\Lambda}_q$) is imposed in Fig. 13(b). For $t < 0$ s without adaptation, the steady-state position error in Fig. 13(a) is $\approx 9°$; it is lower in Fig. 13(b), $\approx 5°$, since the inductance

errors have opposing signs. As the adaptation is enabled at $t = 0$ s, a small residue in steady-state position error, $\approx 2°$, remains due to the error in q-axis flux-maps ($\tilde{L}_q$).

VII. CONCLUSION

A projection vector framework is developed for analysis of sensorless position observers under parametric errors. A position error projection vector APP is proposed having immunity to resistance and inverter errors on MTPA trajectory. The impact of various parametric errors on steady-state position error is analytically examined, revealing dominance of d-axis inductance error.

In the interest of reliability, the projection vector orthogonal to APP is utilized for parameter adaptation. A resistance adaptation is developed to track the temperature induced variations. Alternatively, an inductance adaptation is proposed in the presence of inaccurate flux-maps. Stability analysis to sketch the movement of poles of APP position observer with resistance/inductance adaptation is undertaken.

The proposed technique is experimentally validated on a 1.1 kW SyR machine test bench, demonstrating the immunity of APP to $\tilde{R}_s$ and feasibility of parameter adaptation for improved reliability of position estimation.

REFERENCES

[1] A. Varatharajan, P. Pescetto, and G. Pellegrino, "Sensorless Synchronous Reluctance Motor Drives: A Full-Speed Scheme using Finite-Control-Set MPC in a Projection Vector Framework," *IEEE Transactions on Industry Applications*, vol. 9994, no. c, pp. 1–10, 2020.

[2] Y. D. Yoon, S. K. Sul, S. Morimoto, and K. Ide, "High-bandwidth sensorless algorithm for AC machines based on square-wave-type voltage injection," *IEEE Transactions on Industry Applications*, vol. 47, no. 3, pp. 1361–1370, 2011.

[3] F. Briz and M. W. Degner, "Rotor Position Estimation," *IEEE Industrial Electronics Magazine*, vol. 5, no. 2, pp. 24–36, 2011.

[4] J. Yoo, Y. Lee, and S. Sul, "Back-EMF Based Sensorless Control of IPMSM with Enhanced Torque Accuracy Against Parameter Variation," in *2018 IEEE Energy Conversion Congress and Exposition (ECCE)*, 2018, pp. 3463–3469.

[5] M. Hinkkanen, S. E. Saarakkala, H. A. A. Awan, E. Mölsä, and T. Tuovinen, "Observers for Sensorless Synchronous Motor Drives: Framework for Design and Analysis," *IEEE Transactions on Industry Applications*, vol. 54, no. 6, pp. 6090–6100, 2018.

[6] S. C. Agarlita, I. Boldea, and F. Blaabjerg, "High-frequency-injection-assisted 'active-flux'-based sensorless vector control of reluctance synchronous motors, with experiments from zero speed," *IEEE Transactions on Industry Applications*, vol. 48, no. 6, pp. 1931–1939, 2012.

[7] A. Yousefi-Talouki, P. Pescetto, G. Pellegrino, and I. Boldea, "Combined Active Flux and High-Frequency Injection Methods for Sensorless Direct-Flux Vector Control of Synchronous Reluctance Machines," *IEEE Transactions on Power Electronics*, vol. 33, no. 3, pp. 2447–2457, 2018.

[8] M. Hinkkanen, T. Tuovinen, L. Harnefors, and J. Luomi, "A Combined Position and Stator-Resistance Observer for Salient PMSM Drives: Design and Stability Analysis," *IEEE Transactions on Power Electronics*, vol. 27, no. 2, pp. 601–609, 2012.

[9] D. Liang, J. Li, and R. Qu, "Sensorless Control of Permanent Magnet Synchronous Machine Based on Second-Order Sliding-Mode Observer With Online Resistance Estimation," *IEEE Transactions on Industry Applications*, vol. 53, no. 4, pp. 3672–3682, 2017.

[10] Y. Inoue, Y. Kawaguchi, S. Morimoto, and M. Sanada, "Performance Improvement of Sensorless IPMSM Drives in a Low-Speed Region Using Online Parameter Identification," *IEEE Transactions on Industry Applications*, vol. 47, no. 2, pp. 798–804, 2011.

[11] P. Pescetto and G. Pellegrino, "Automatic Tuning for Sensorless Commissioning of Synchronous Reluctance Machines Augmented with High-Frequency Voltage Injection," *IEEE Transactions on Industry Applications*, vol. 54, no. 5, pp. 4485–4493, 2018.

[12] A. Varatharajan, P. Pescetto, and G. Pellegrino, "Sensorless Self-Commissioning of Synchronous Reluctance Machine with Rotor Self-Locking Mechanism," in *2019 IEEE Energy Conversion Congress and Exposition (ECCE)*, 2019, pp. 812–817.

[13] T. Tuovinen, H. A. A. Awan, J. Kukkola, S. E. Saarakkala, and M. Hinkkanen, "Permanent-Magnet Flux Adaptation for Sensorless Synchronous Motor Drives," in *2018 IEEE 9th International Symposium on Sensorless Control for Electrical Drives (SLED)*, 2018, pp. 138–143.

[14] M. Hasegawa and K. Matsui, "Position sensorless control for interior permanent magnet synchronous motor using adaptive flux observer with inductance identification," *IET Electric Power Applications*, vol. 3, no. 3, pp. 209–217, 2009.

[15] A. Varatharajan and G. Pellegrino, "Sensorless Synchronous Reluctance Motor Drives: A General Adaptive Projection Vector Approach for Position Estimation," *IEEE Transactions on Industry Applications*, vol. 56, no. 2, pp. 1495–1504, 2020.

[16] ——, "Sensorless Synchronous Reluctance Motor Drives: A Sensitivity Analysis Framework and Design to Achieve Stator Resistance Immunity," in *2019 IEEE 10th International Symposium on Sensorless Control for Electrical Drives (SLED)*, 2019, pp. 1–6.

[17] I. R. Bojoi, E. Armando, G. Pellegrino, and S. G. Rosu, "Self-commissioning of inverter nonlinear effects in AC drives," *2012 IEEE International Energy Conference and Exhibition, ENERGYCON 2012*, pp. 213–218, 2012.

[18] E. Armando, R. I. Bojoi, P. Guglielmi, G. Pellegrino, and M. Pastorelli, "Experimental identification of the magnetic model of synchronous machines," *IEEE Transactions on Industry Applications*, vol. 49, no. 5, pp. 2116–2125, 2013.

[19] A. Varatharajan, S. S. Cruz, H. Hadla, and F. Briz, "Predictive torque control of SynRM drives with online MTPA trajectory tracking and inductances estimation," in *2017 IEEE International Electric Machines and Drives Conference (IEMDC)*, 2017, pp. 1–7.

[20] Y. Park and S. K. Sul, "Implementation Schemes to Compensate for Inverter Nonlinearity Based on Trapezoidal Voltage," *IEEE Transactions on Industry Applications*, vol. 50, no. 2, pp. 1066–1073, 2014.